International Journal of Heat and Fluid Flow 29 (2008) 1295–1308

Contents lists available at ScienceDirect

International Journal of Heat and Fluid Flow

journal homepage: www.elsevier.com/locate/ijhff

# Multiple steady fluid flows in a slot-ventilated enclosure

Fu-Yun Zhao *, Di Liu, Guang-Fa Tang

*College of Civil Engineering, Hunan University, Changsha, Hunan Province 410082, PR China*

ARTICLE INFO

*Article history:*
Received 18 October 2007
Received in revised form 24 June 2008
Accepted 26 June 2008
Available online 5 August 2008

*Keywords:*
Enclosure flow
Slot-ventilation
Multiple solutions
Computational fluid dynamics

ABSTRACT

Present work numerically investigates three-dimensional non-linear aerodynamic structures of airflow in a slot-ventilated compartment with three ports. A numerical code based on Reynolds average Navier–Stokes equations and Reynolds stress turbulence model was validated, and successfully conducted for simulating the airflow in the studied room. Numerical results are particularly presented to illustrate the effects of the inlet airflow velocity, enclosure width, supplying ports elevation and Reynolds number on the multiple flow patterns and the associated ventilation flow rate and blowing-axial momentum decay for equal-magnitude opposite jet flows. It is shown that the room airflow rate and the shift of jet flow interface can be promoted or inhibited, depending strongly on the jet velocity, enclosure width and elevation of supplying ports.



## 1. Introduction

Confined convection is of essential importance for a variety of practical applications, such as air-supply in offices or residential buildings, the cooling of electronic devices, solar collectors, and the air-conditioning of vehicle and aircraft cabins (Papanicolaou and Jaluria, 1992, 1995; Calmidi and Mahajan, 1998; Bilgen and Yamane, 2004; Mahmud and Pop, 2006; Chen et al., 2006). The primary goals in ventilation include provision of sufficient fresh air and satisfactory velocity. In some cases, multi-diffusers would supply the fresh air into the same zone, provided that the ventilation flow is appropriately manipulated. In this work, we focus on isothermal ventilation that develops when air is supplied by the slot ports at both sides, and exits from the top of the room. Actually, buoyant plumes would develop around any warm object in the room such as people and electrical equipment, which is not in consideration in this work.

However, this basic steady state regime of that ventilation in which fresh air is drawn through the bottom vents and displaces the indoor, old air out through the top vent may not be unique. Under some situations, it is reasonable to expect multiple steady states of the ventilation flow. This is particularly true if the air flow rates of the side ports close to each other.

In recent years, several investigations have shown that there can be multiple solutions in two-dimensional natural convection and mixed convection problems (Aidun et al., 1991; Mamou et al., 1995, 1998; Kuhlmann et al., 1997; Calmidi and Mahajan, 1998; Mamou, 2002; Bourich et al., 2004a,b; Mahmud and Pop, 2006; Chen et al., 2006; Li et al., 2006; Zhao et al., 2007a, 2008a). They have analyzed a number of governing factors in natural or mixed convections, including discrete thermal and solutal sources, fluid property, supplying air velocity, size and position of ports, closed or open cavities. However, the bifurcations of three-dimensional fluid flow in slot-ventilated enclosures have not been considered. Three-dimensionality is more realistic in building ventilation, especially when the ventilation forces are opposing and are of comparable magnitude.

The present study is dedicated to the numerical investigations of the multiple flow states in a three-dimensional ventilated room. It was found that secondary flow structures evolve on planes perpendicular to the main flow rotation that cannot be predicted and visualized by two-dimensional models. Only the turbulent flow of beyond the critical Reynolds number is considered in the present work.

## 2. Physical configuration and model

As shown in Fig. 1, three-dimensional ventilated room was modeled with a rectangular parallelepiped width $W$ m ($x$-direction), a height $H$ m ($z$-direction) and a span $B$ m ($y$-direction). The enclosure used in the computational fluid dynamics (CFD) simulations comprised three openings. The openings were all of equal area $S \times S$ m$^2$. Two inlet ports were located at each sidewall and positioned symmetrically about the mid-plane through the center of the floor ($x = 0$); the distance between the center of the inlet ports and the bottom wall was $C$. The outlet vent was centered at the top plane $z = H$.

The air that fills and flows through this enclosure is a Newtonian fluid with nearly constant density $\rho$ and viscosity $\mu$. Due to

* Corresponding author. Tel.: +86 731 8822760; fax: +86 731 8822667.
*E-mail addresses:* zfycfdnet@163.com (F.-Y. Zhao), liudi66@163.com (D. Liu), gftangcfd@163.com (G.-F. Tang).

0142-727X/$ - see front matter © 2008 Elsevier Inc. All rights reserved.
doi:10.1016/j.ijheatfluidflow.2008.06.005

**Nomenclature**

| | |
|---|---|
| $A$ | hydraulic diameter |
| AU | average blowing-axis velocity |
| $B$ | enclosure span |
| FR | air flow rate |
| $H$ | enclosure height |
| $I$ | turbulent intensity |
| $k$ | turbulent kinetic energy |
| $p$ | pressure |
| $Re$ | Reynolds number |
| $S$ | size of vent ports |
| $t$ | time |
| $u$, $v$, $w$ | velocity components |
| $W$ | enclosure width |
| $x$, $y$, $z$ | Cartesian coordinates |

*Greek symbols*

| | |
|---|---|
| $\delta$ | Kronecker delta |
| $\varepsilon$ | turbulent energy dissipation rate |
| $\mu$ | dynamic viscosity |
| $\nu$ | kinematical viscosity |
| $\nu_t$ | turbulent viscosity |
| $\rho$ | fluid density |
| $\tau$ | shear stress |
| $\kappa^*$ | von Karman's constant |

*Subscripts*

| | |
|---|---|
| L | left supplying port |
| R | right supplying port |
| $i$, $j$, $k$ | vector directions in $x$, $y$ and $z$ |

the Coanda effect, this design should allow to the issuing confined wall jet to entrain the air in the whole enclosure. Combination of free turbulent shear flows and near-wall effect often complicates the airflow in the confined enclosure. Simultaneously, interactions between airflow and pressure gradient result in the primary and secondary recirculations including high streamline curvature effect. Thus, Reynolds stress model (RSM) is adopted to improve the accuracy of prediction (Launder et al., 1975; Hanjalic and Launder, 1976; Chen, 1995, 1996; Moureh et al., 2002; Moureh and Flick, 2003, 2004, 2005; Tapsoba et al., 2007; Liu et al., 2008a). A computational fluid dynamics code was developed to solve the room airflow. The mathematical model for continuity and momentum conservation equations is given as follows:

Continuity equation

$$\frac{\partial}{\partial x_i}(\rho\overline{u_i}) = 0 \tag{1}$$

Momentum equation

$$\frac{\partial \rho\overline{u_i}}{\partial t} + \frac{\partial}{\partial x_j}(\rho\overline{u_i}\overline{u_j}) = -\frac{\partial p}{\partial x_i} + \frac{\partial}{\partial x_j}\left(\mu\frac{\partial \overline{u_i}}{\partial x_j} - \rho\overline{u_i'u_j'}\right) \tag{2}$$

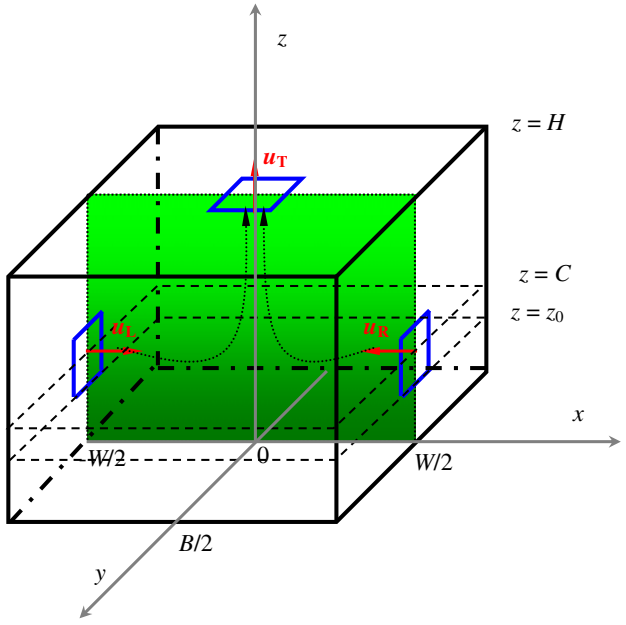


**Fig. 1.** Schematic view of the full scale ventilated room with three ports of the same dimensions.

In the above equations, $\overline{u_i}$ and $u_i'$, respectively, represent the time-mean velocity component and the fluctuating velocity component in the $x_i$ direction. While, $\overline{u_i'u_j'}$ is the unknown Reynolds stress.

A full RSM closure generally consists of six transport equations for the Reynolds stresses (Launder et al., 1975; Hanjalic and Launder, 1976; Chen, 1996; Liu et al., 2008a). The Reynolds stress-transport equations include the diffusion, production, and pressure strain terms. The transport equation for Reynolds turbulent stress gives rise to,

$$\frac{\partial \rho\overline{u_i'u_j'}}{\partial t} + \rho\overline{u_k}\frac{\partial \overline{u_i'u_j'}}{\partial x_k} = D_{ij} + \rho G_{ij} + \overline{p\left(\frac{\partial u_i'}{\partial x_j} + \frac{\partial u_j'}{\partial x_i}\right)} - 2\mu\overline{\frac{\partial u_i'}{\partial x_k}\frac{\partial u_j'}{\partial x_k}} \tag{3}$$

where the diffusive transport term $D$ can be modeled by the assumption that the rate of transport of Reynolds stresses by diffusion is proportional to the gradients of Reynolds stresses. Here, term $D$ is represented by a simplified form of the generalized gradient diffusion hypothesis as (Lien and Leschziner, 1994),

$$D_{ij} = \frac{\partial}{\partial x_k}\left(\frac{\mu_t}{\sigma_k}\frac{\partial}{\partial x_k}\left(\overline{u_i'u_j'}\right)\right) \tag{4}$$

The production term $G$ is given in its exact form,

$$G_{ij} = -\overline{u_i'u_k'}\frac{\partial \overline{u_j}}{\partial x_k} - \overline{u_j'u_k'}\frac{\partial \overline{u_i}}{\partial x_k} \tag{5}$$

The pressure–strain term, consisting of the linear return-to-isotropy, is modeled by Launder et al. (1975) as,

$$\overline{p\left(\frac{\partial u_i'}{\partial x_j} + \frac{\partial u_j'}{\partial x_i}\right)} = -C_1\rho\frac{\varepsilon}{k}\left(\overline{u_i'u_j'} - \frac{2}{3}\delta_{ij}k\right) - C_2\rho\left(G_{ij} - \frac{2}{3}\delta_{ij}G\right) \tag{6}$$

where $G = 0.5G_{ii}$, whereas the constants are maintained at $C_1 = 1.8$, $C_2 = 0.60$. The pressure–strain interactions constitute at the same time the most difficult term in Eq. (3) and the most important one to model accurately.

The dissipation term is modeled by assuming isotropy of the small dissipative eddies. It is set so that it only affects the normal Reynolds stresses ($i = j$) in equal measure. This can be achieved by

$$2\mu\overline{\frac{\partial u_i'}{\partial x_k}\frac{\partial u_j'}{\partial x_k}} = \frac{2}{3}\delta_{ij}\rho\varepsilon \tag{7}$$

where the Kronecker delta $\delta_{ij}$ is given by $\delta_{ij} = 1$ if $(i = j)$, and $\delta_{ij} = 0$ if $(i \neq j)$; the dissipation rate $\varepsilon$ is computed through the following transport equation:

$$\frac{\partial \rho\varepsilon}{\partial t} + \rho\overline{u_j}\frac{\partial \varepsilon}{\partial x_j} = C_{\varepsilon 1}\frac{\varepsilon}{k}\left(-\rho\overline{u_i'u_j'}\frac{\partial \overline{u_i}}{\partial x_j}\right) - C_{\varepsilon 2}\frac{\rho\varepsilon^2}{k} + \frac{\partial}{\partial x_j}\left(\left(\mu + \frac{\mu_t}{\sigma_\varepsilon}\right)\frac{\partial \varepsilon}{\partial x_j}\right) \tag{8}$$

The empirical coefficients appearing in the above equations, $C_{\varepsilon 1}$, $C_{\varepsilon 2}$, $\sigma_k$ and $\sigma_\varepsilon$ are 1.44, 1.92, 1.00 and 1.30, respectively. The eddy viscosity concept is adopted to relate the eddy viscosity $\mu_t$ to the turbulent kinetic energy $k$ and its rate of dissipation $\varepsilon$,

$$\mu_t = \rho C_\mu k^2/\varepsilon \tag{9}$$

Here, $C_\mu = 0.09$.

## 3. Boundary condition and dimensional scale

The non-slip impermeable conditions are imposed on all the solid walls. The flow through both inlet ports is purely horizontal (forming a jet), and the velocity components ($u_L$ and $u_R$), kinetic energy of turbulence ($k_L$ and $k_R$) and the energy dissipation rate ($\varepsilon_L$ and $\varepsilon_R$) of this stream are uniform over the cross-section of the inlet ports. For the left and right inlets,

$$k_L = 3/2(u_L I_{ox})^2, \quad \varepsilon_L = C_\mu^{0.75} k_L^{1.50}/(0.07 A_L) \tag{10a}$$

$$k_R = 3/2(u_R I_{ox})^2, \quad \varepsilon_R = C_\mu^{0.75} k_R^{1.50}/(0.07 A_R) \tag{10b}$$

where $I_{ox} = 10\%$ represents the turbulence intensity of the $x$-component of velocity at the inlet as obtained from experiments (Craft et al., 1993; Versteeg and Malalasekera, 1999), whereas $A$ represents the hydraulic diameter of the inlet section. For the RSM, the turbulence is assumed to be isotropic, $\overline{u_i' u_j'} = \frac{2}{3} k_R \delta_{ij}$.

The turbulence model is only valid in fully turbulent regions. Close to the wall, where viscous effects become dominant, these models are used in conjunction with wall functions (Launder and Spalding, 1974; Launder, 1988). For this study, the conventional equilibrium logarithmic law governing the wall is used. Assuming that the point $P$ is sufficiently remote from its adjacent grid point $W$, which lies on the wall; so much greater in fact that the viscous effects are entirely overwhelmed there by the turbulent ones. The momentum fluxes to the wall are then supposed to obey the relations,

$$\frac{u_P}{\tau_w/\rho} C_\mu^{1/4} k_P^{1/2} = \frac{1}{\kappa^*} \ln[E y_P^+] \tag{11}$$

where the wall-coordinate $y^+$ is given by,

$$y_P^+ = \frac{\rho C_\mu^{1/4} y_P \sqrt{k}}{\mu} \tag{12}$$

Here $u_P$, $\tau_w$, and $y_P$ are, respectively, the time-average velocity of the fluid at point $P$ along the wall, the shear stress on the wall in the direction of the velocity $u_P$, and the distance of the point $P$ from the wall. $E$ is a function of the wall roughness, approximately equal to 9.0 for a smooth wall. The von Karman's constant $\kappa^*$ is in the range of 0.4–0.42. When calculating $k_P$, it is of course necessary to assign a value for the average energy dissipation rate over the control volume.

The location of the cell center away from the wall must be such that $y_P^+ > 11.3$ for Eq. (11) to be valid. To evaluate the dissipation rate in the logarithmic layer, we take,

$$\varepsilon = \frac{C_\mu^{3/4} k^{3/2}}{\kappa^* y} \tag{13}$$

Within the viscous sub-layer we adopt the following expression:

$$\varepsilon = \rho C_\mu \frac{k^2}{\mu} \tag{14}$$

With (13) and (14), we can compute the dissipation rate over half of the near-wall cell,

$$\varepsilon = \frac{1}{y_P} \int_0^{y_P} \varepsilon \mathrm{d}y = \begin{cases} C_\mu^{3/4} k_P^{3/2} \frac{y_P^+}{y_P}, & y_P^+ \leqslant 11.3 \\ C_\mu^{3/4} k_P^{3/2} \frac{\ln(E y_P^+)}{\kappa^* y_P}, & y_P^+ > 11.3 \end{cases} \tag{15}$$

At the top outflow port, pressure is assumed to be uniform and zero-gradient is applied for all transport variables.

Recognizing that the convection term must maintain balance and considering the ranges of governing parameters in the present work (Zhao et al., 2006), the following dimensionless variables are used,

$$X_i = x_i/H, (U_i) = (u_i)/u_R, \quad t^* = t/(H/u_R), \quad p^* = p/\rho u_R^2,$$
$$k^* = k/u_R^2, \quad \varepsilon^* = \varepsilon H/u_R^3 \tag{16}$$

The superscript $^*$ represents the dimensionless variables. The corresponding Reynolds number is defined as,

$$Re = \rho u_R H/\mu \tag{17}$$

where enclosure height $H$ and right inlet velocity $u_R$ are utilized for length scale and velocity scale, respectively. Usually, $H = 2.0$ m is set in the present work. The Reynolds number is in a range of $10^2$ to $10^6$, and the air kinetic viscosity is $1.5 \times 10^{-5}$ m$^2$/s resulting in right inlet velocity varies from $7.5 \times 10^{-4}$ m/s to 7.5 m/s. The data in the following numerical simulations are non-dimensional results without special illustration.

## 4. Numerical method and code validation

Eqs. (1)–(12) are discretized using staggered, non-uniform control volumes (Patankar, 1980). In order to minimize the numerical diffusion errors, QUICK (Hayase et al., 1992) and CDS schemes are used in approximating the advection and diffusion terms, respectively. To alleviate the convergence problems, the method is implemented in the solution procedure using the deferred correction approach (Zhao et al., 2006, 2007a, 2008a; Liu et al., 2008a). SIMPLE algorithm is used to couple the momentum and continuity equations (Patankar, 1980). To obtain better convergence properties, the unsteady terms in these equations were implicitly treated and hence approximated by backward differencing. The pressure correction equation is derived from the continuity equation to enforce the local mass balance (Patankar, 1980; Liu et al., 2008a). Consequently, the finite volume representations for the governing equations became fully implicit. For each time step, the momentum equations and other scalar equations are solved by applying an iteration of the strongly implicit procedure (SIP) of Stone (1968), which is extended here to handle three-dimensional problems.

A sine function is used for the orthogonal grid distribution, with denser grid clustering near the boundaries and ports (Chen et al., 2006; Liu et al., 2008a). Simultaneously, the relevant grid generation is strictly symmetric about the mid-plane through the center of the floor ($X = 0$). The appropriate grid size was selected after several numerical accuracy tests for different geometries. For example, the grid size tested ranged between $41 \times 21 \times 31$ and $81 \times 51 \times 61$ for $W/H = 1.5$ and $C/H = 0.25$. The results showed that grid independence was achieved above $71 \times 31 \times 41$, showing acceptable differences in flow rate. Therefore, all calculations carried out are based on $71 \times 31 \times 41$ control volumes for that geometry.

The solutions for the pressure correction equation were iterated until the local mass balance was achieved to a satisfactory degree (Patankar, 1980; Liu et al., 2008a). The solutions for the problem were marched from the initial state to the final steady state. To ensure convergence of the numerical algorithm, the following criteria is applied to all dependent variables over the solution domain,

$$\frac{\sum \left| \phi_{ijk}^m - \phi_{ijk}^{m-1} \right|}{\sum \left| \phi_{ijk}^m \right|} < 10^{-7} \tag{18}$$

where $\phi$ represents a dependent variable, i.e., $U$, $V$, $W$, $P$, $K$ or $E$, the indexes $i$, $j$, $k$ indicate a grid point and the index $m$ the current iteration.

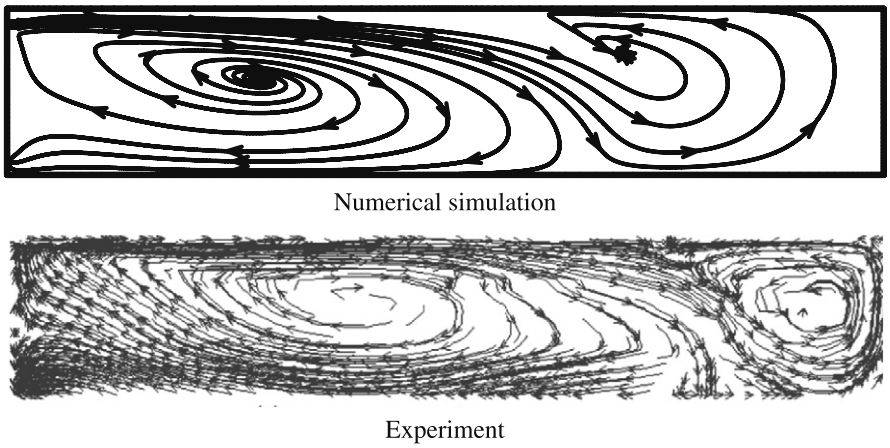


**Fig. 2.** Airflow pattern on the symmetry plane: comparison between experiment (Moureh and Flick, 2005) and our numerical results.

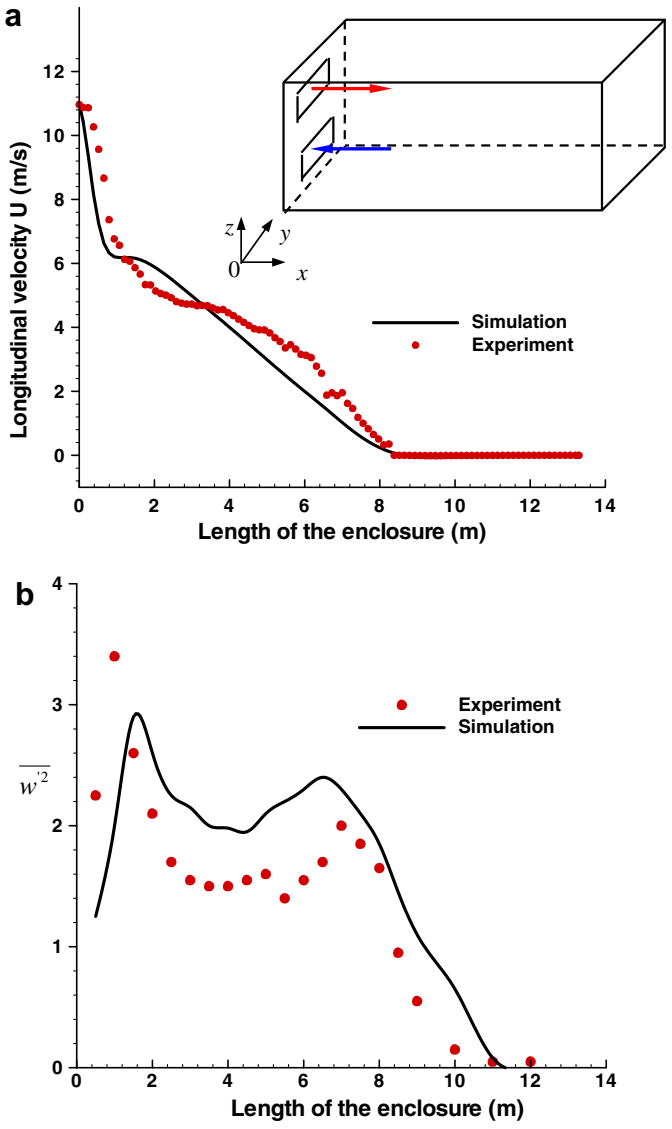


**Fig. 3.** Comparison between experiment and our numerical results in terms of jet velocity (a) and the mean square of the fluctuating velocity (b) along the blowing axis.

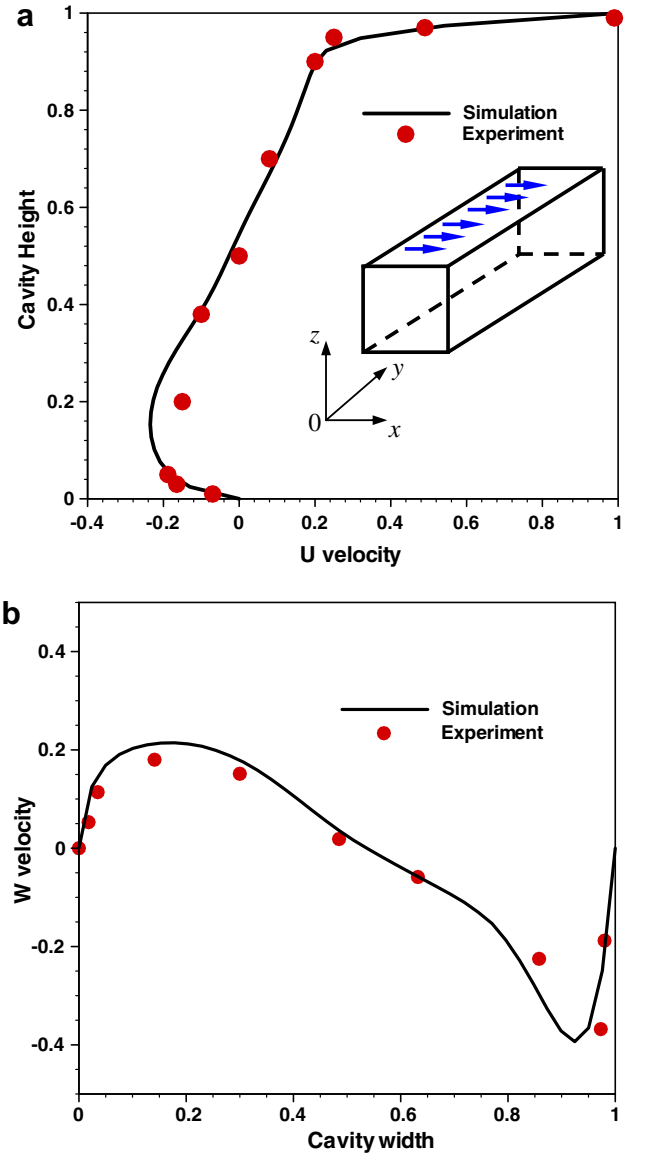


**Fig. 4.** Comparison between RSM and experimental results in terms of centerline mean velocity profiles: simulation profile at $Z = 0.28$ plane and experimental data measured at mid-span plane. (a) $U$ velocity and (b) $W$ velocity.

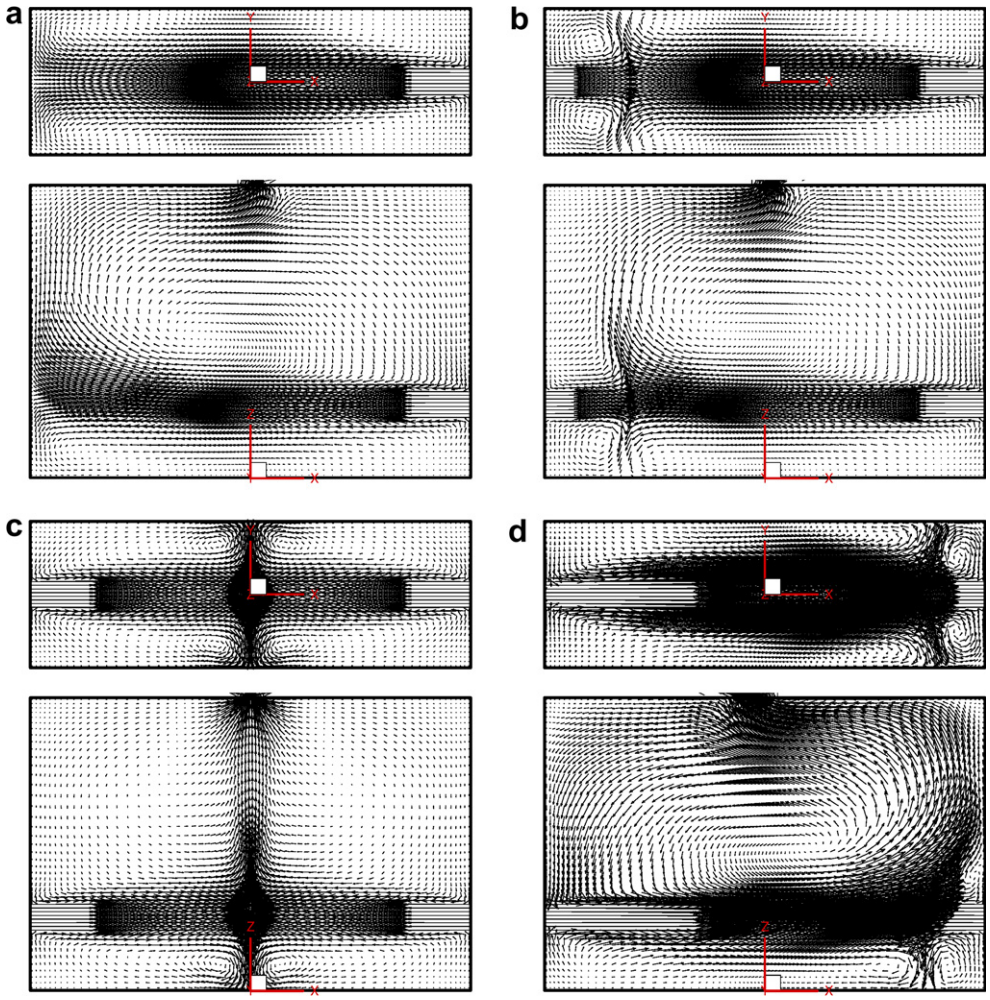


**Fig. 5.** Vector flow charts for $Re = 2 \times 10^5$, $W/H = 1.5$ and $C/H = 0.25$. (a) $U_L = 0.0$, AU = −0.6716, UC = −0.7267, FR = 0.0135; (b) $U_L = 0.5$, AU = −0.5383, UC = −0.7421, FR = 0.0155; (c) $U_L = 1.0$, AU = −0.0025, UC = −0.0151, FR = 0.0155; (d) $U_L = 2.5$, AU = 1.4765, UC = 1.8420, FR = 0.0359.

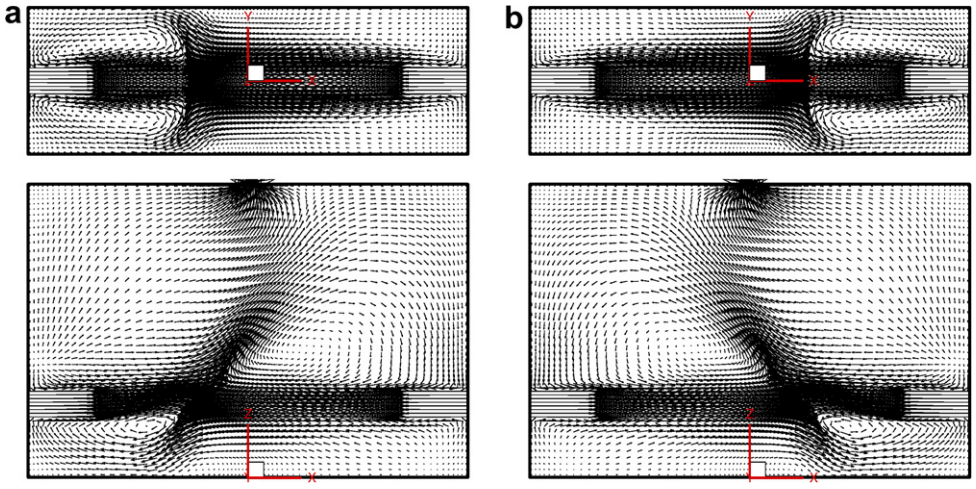


**Fig. 6.** Vector flow charts for $Re = 2 \times 10^5$, $W/H = 1.5$ and $C/H = 0.25$. (a) $U_L = 1.0$, AU = −0.2632, UC = −0.6938, FR = 0.0244 and (b) $U_L = 1.0$, AU = 0.2541, UC = 0.6890, FR = 0.0243.

Additionally, a remark must be made with regard to the numerical procedure, which would also apply to other cases where any integration in time is used to solve a problem with multiple linearly stable steady states. Each of these states has its own basin of attraction and only initial conditions within this basin will evolve to the desired steady state within it. Thus, initial conditions have

to be chosen carefully for each numerical run. So when multiple steady states do exist, initial conditions determine the final steady state achieved. If suitable initial conditions are not chosen, the numerical solution evolves to some other state, which could be the natural state or multi-cellular flow. Under such conditions, one has to make a large number of computations with very small tuning of governing parameter after each computation and use the previous state as initial condition to assure convergence to the desired anti-natural state.

The current numerical method has been successfully used in a series of recent papers, including slot-ventilated enclosure flow (Chen et al., 2006; Liu et al., 2008a), conjugate heat transfer (Zhao et al., 2006, 2007b,c; Liu et al., 2008b), double diffusive natural convection in gaseous enclosures (Zhao et al., 2007a), and porous enclosures (Zhao et al., 2007d, 2008a,b; Liu et al., 2008c), and transient convective flows (Liu et al., 2008b; Zhao et al., 2007e).

Further, before applying the numerical scenario simulations to the proposed problem, the present turbulent airflow numerical model was verified by a three-dimensional trailer given by Moureh and Flick (2005), which provides reliable experimental data of velocity. The details of the trailer configuration would be found in their paper (Moureh and Flick, 2005). Fig. 2 depicts the comparisons of streamlines related to the mean flow field on the symmetry plane in the enclosure between experiments and numerical simulation. These flow patterns are consistent with the experimental data of Moureh and Flick (2005). Fig. 3a presents the decay of the jet velocity. It can be observed that the wall jet separates from the ceiling at approximately $X/L = 8.5/13.3$. The primary recirculation located in the front part of the enclosure delimits the reach and the action of the inlet jet. The results show good agreement of distributions of the simulated and measured data. The variation of the mean square of the longitudinal fluctuating velocity along the blowing axis is also illustrated in Fig. 3b. Due to turbulent jet expansion and high gradient of velocities near separation, double-peak structure is apparently observed for experimental data and simulations (Moureh and Flick, 2005). Furthermore, the turbulence model may not accurately calculate the turbulent energy. Therefore, it is not surprising to see the discrepancies between the computed profiles and measured data.

The validation was also carried out with the comparison between the simulation and the experimental data provided by Koseff and Street (1984). The cavity geometry was modeled with a cavity width 1.0 ($x$-direction), a height 1.0 ($z$-direction) and a span 1.5 ($y$-direction). One boundary of the span was modeled as a plane of symmetry ($Y = 0.0$) and the other a solid end-wall ($Y = 1.5$). Examining the comparisons between the computed centerline velocity profiles and the experimental results was conducted and shown in Fig. 4 with $Re = 10^4$. Sensitivity analysis indicated that the flow characteristics do not change, as Reynolds number does not exceed $10^4$. The averaged error (as compared to the date) was less than 10%.

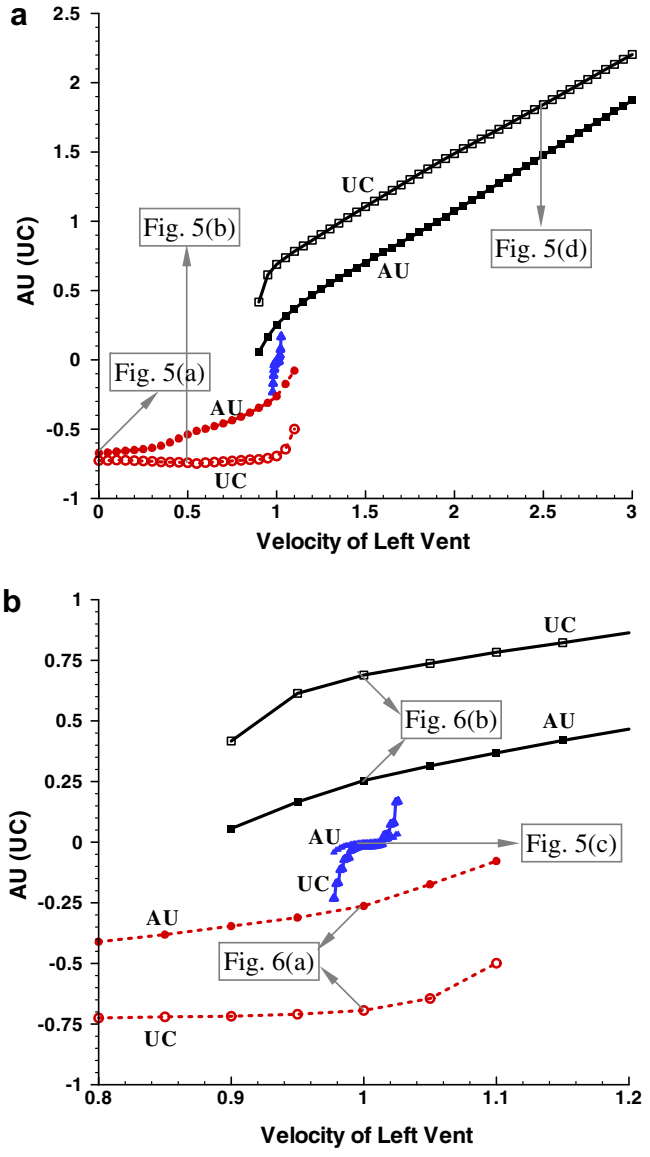


**Fig. 7.** Effect of left jet velocity $U_L$ on the average blowing velocity AU, central vector component UC and average flow rate FR for $Re = 2 \times 10^5$, $W/H = 1.5$ and $C/H = 0.25$. Fig. 7b is enlarged from Fig. 7a.

## 5. Ventilation efficiency and evaluation

The flow rate $FR$ is introduced in terms of the volume $Vol_Z$ comprised between $Z_0 = (C - S/2)/H$ section and the floor of the room,

$$FR = \frac{0.5 \int_{S_Z} |W|_{Z_0} \, ds}{S_Z} \tag{19}$$

The flow rate $FR$ is not only composed of the air entering the volume $Vol_Z$ but also the air flowing out it. They are obtained, respectively, by the following integrations,

$$FRI = \frac{0.5 \int_{S_Z} (|W| - W)_{Z_0} \, ds}{S_Z}, \quad FRO = \frac{0.5 \int_{S_Z} (|W| + W)_{Z_0} \, ds}{S_Z} \tag{20}$$

Concerning the mass conservation and the boundary conditions of that volume, the equality $FR = FRI = FRO$ should be set up usually for each steady state.

The average horizontal velocity along the jet axis AU can be defined as,

$$AU = \sum_{i=1}^{NI} U_i \cdot \Delta X_i / \sum_{i=1}^{NI} \Delta X_i \tag{21}$$

where $U_i$, $\Delta X_i$ and $NI$ represent the $U$-velocity on the blowing axis ($-W/2H < X < W/2H, Y = 0, Z = C/H$), cell spacing and the total number of nodes of $x$-direction, respectively. Aforementioned grid generation is strictly symmetric of the vertical mid-plane $X = 0$, which means the number of nodes from $(-W/2H, 0, C/H)$ to $(0, 0, C/H)$ is exactly the same with that from $(0, 0, C/H)$ to $(W/2H, 0, C/H)$. Thus, the value of AU can measure the horizontal shift of the interface between both fronts of opposite jet flows. Particularly, for component

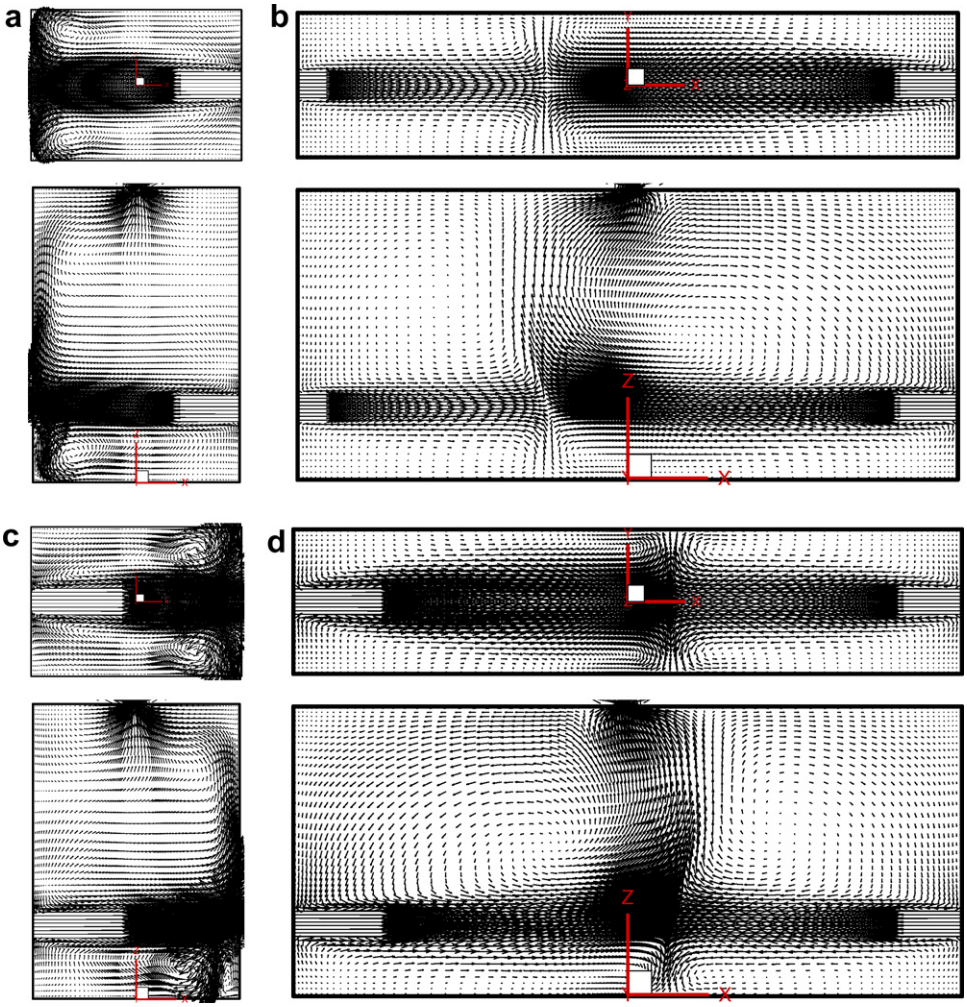


**Fig. 8.** Effect of $W$ on the vector flow for $Re = 2 \times 10^5$ and $C/H = 0.25$. (a) $W/H = 0.7$, and $U_L = 0.5$, AU = −0.7712, UC = −0.9783, FR = 0.0281; (b) $W/H = 2.3$, and $U_L = 0.5$, AU = −0.3117, UC = −0.4725, FR = 0.0102; (c) $W/H = 0.7$, and $U_L = 1.5$, AU = 1.0914, UC = 1.4720, FR = 0.0417 and (d) $W/H = 2.3$, and $U_L = 1.5$, AU = 0.3133, UC = 0.6136, FR = 0.0154.

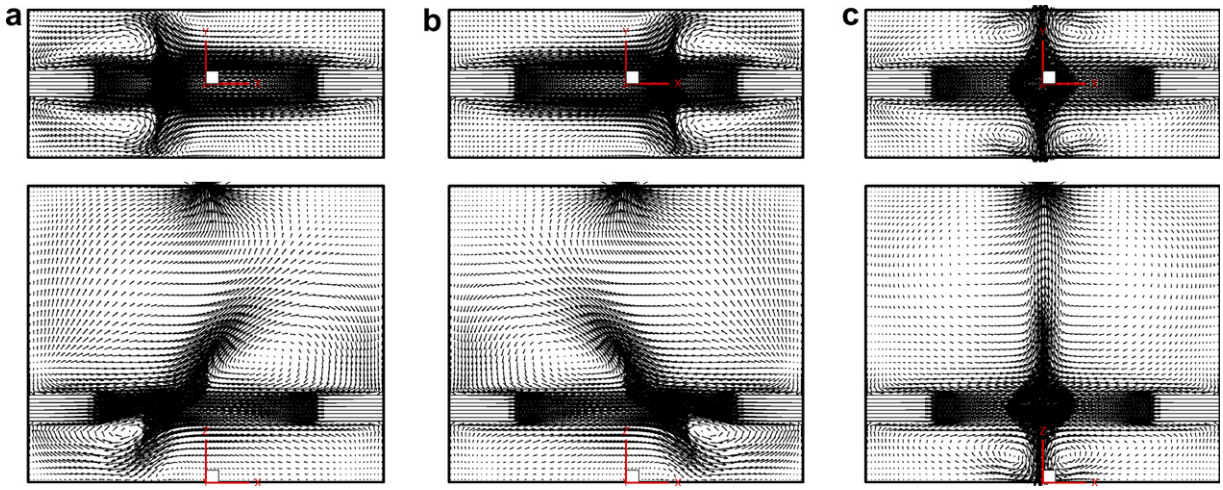


**Fig. 9.** Multiple steady flows for $Re = 2 \times 10^5$, $C/H = 0.25$, $W/H = 1.2$ and $U_L = 1.0$. (a) Obtained from lower $U_L$ (0.0), AU = −0.2288, UC = −0.7685, FR = 0.0295; (b) obtained from higher $U_L$ (2.0), AU = 0.2297, UC = 0.7688, FR = 0.0295 and (c) from rest state, AU = −0.0108, UC = −0.0896, FR = 0.0226.

$U$ along the blowing jet line $(-W/2H < X < W/2H, 0, C/H)$ being symmetric of $X = 0$, AU tends to be zero. Additionally, horizontal vector component on the central point of the jet axis, UC, can also illuminate the symmetry and the interface shift of the opposite jets

$$UC = U(X = 0, Y = 0, Z = C/H) \tag{22}$$

As expected, UC would also tend to be zero as the component $U$ along the blowing jet line being symmetric of $X = 0$.

Actually, the governing system of Eqs. (1) and (2), and the equal-magnitude jets admit two-spatial symmetries in the solution. Firstly, the solution can be symmetric in the blowing jet line $(X, 0, C/H)$ and it has been numerically denoted by AU and UC. Secondly, it can be symmetric with respect to the vertical mid-plane $X = 0$, i.e.,

$$U(a, Y, Z) = -U(-a, Y, Z) \tag{23a}$$

$$V(a, Y, Z) = V(-a, Y, Z) \tag{23b}$$

$$W(a, Y, Z) = W(-a, Y, Z) \tag{23c}$$

However, the symmetric flow structures are not the sole one for realistic fluid flow. When different initial conditions were achieved, other flow paths would emerge.

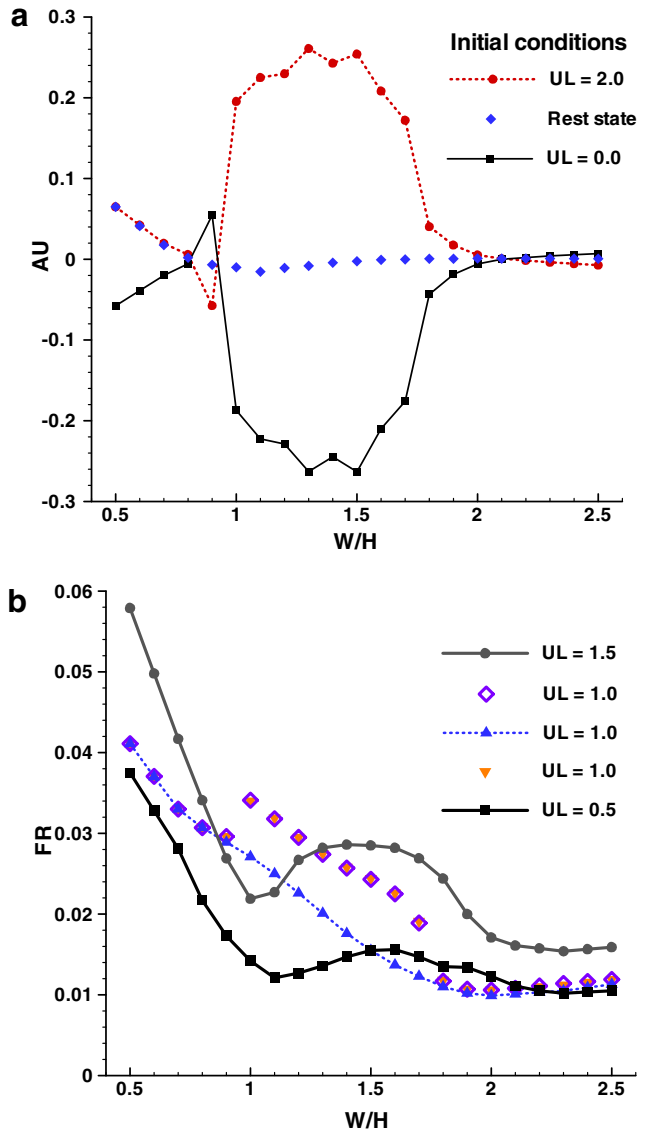


**Fig. 10.** (a) AU as a function of $W/H$ for $U_L = 1.0$. (b) FR as a function of $W/H$ Average blowing velocity AU and average flow rate FR as functions of dimensionless enclosure width $W/H$ with parameter $U_L$, and $Re = 2 \times 10^5$.

## 6. Numerical results and discussion

As was already noted above, the problem under investigation is governed by six groups: the Reynolds number $Re$, left inlet velocity $U_L$, enclosure geometries $W/H$ and $B/H$, the vertical position of the slots $C/H$, and the size of three ports $S/H$. It is a formidable task to perform computations covering wide ranges of all these parameters. Instead, enclosure span and size of three ports are maintained constant at $B/H = 0.5$ and $S/H = 0.1$, respectively. Attention is, therefore, focused herein on the effects of the left inlet velocity $U_L$, width of the enclosure $W/H$, distance between the center of supplying ports and the bottom wall $C/H$, and Reynolds number $Re$ on the ventilated air flow. Without special explanation, vectors depicted below are at horizontal XOY plane $(Z = C/H)$ and vertical XOZ mid-plane $(Y = 0)$, respectively.

### 6.1. Effect of left jet flow

Airflow Reynolds number $Re$, geometries $W/H$ and $C/H$ are maintained at $2 \times 10^5$ ($u_R = 1.5$ m/s), 1.5, and 0.25, respectively. The velocity of left jet $U_L$ is varied from 0.0 to 3.0 (absolute value $u_L$ from 0 to 4.5 m/s). Airflow pattern and velocity characteristics in this enclosure have some original features that should be highlighted.

Differing from the unbounded wall jet, for the jet flow in an enclosure, the maintenance of the jet at floor level is more complex because it involves the action of the pressure gradient in horizontal and vertical directions. Observing from Fig. 5a, when the left jet flow was not started up, the right jet flow spreads at the blowing level and then rises along the left wall. Simultaneously, the jet induces the surrounding air and the induction causes a reverse flow in the layer between port and the floor. This flow pattern is similar to the traditional displacement ventilation system for supplying cooling air from a low level diffuser (Chen et al., 2006). When the left jet flow increases up to $U_L = 0.5$, shown in Fig. 5b, the right jet flow can maintain the original flow structure except that the upward flow path is shifted rightward pushed by the left jet airflow. As expected, the average horizontal velocity along the jet axis AU decreases in absolute values. However, the central vector component UC increases due to the horizontal path of right jet flow dwindles. Owing to the promotion of airflow rate, the less-mixing process causes the velocity profile to nib with distance and in turn implies the increasing of the total flux of momentum. When the left jet flow increases to the level identical to the right jet flow, $U_L = 1.0$ (Fig. 5c), the symmetrical flow structures satisfying Eqs. (23a)–(23c) span now completely the enclosure. Observing from the horizontal XOY plane, two pairs of counter-rotating cells form in the back and front sides, respectively. When the left jet flow increases abruptly to $U_L = 2.5$, shown in vertical XOZ plane of Fig. 5d, the counter-clockwise eddy flow above the blowing axis has been conversely changed to clockwise one.

Aforementioned flow charts are all achieved for unique steady solution, and their initial conditions are the rest state $U = V = W = 0$. However, multiple steady solutions are possible when different initial conditions are used, particularly for the equal-magnitude jets flow. As shown in Figs. 6 and 5c, three possible solutions are obtained for $U_L = 1$. The first solution, Fig. 6a, obtained by using the flow configuration of Fig. 5a as initial conditions, is observed to have negative values of AU and UC, which is similar to that in Fig. 5a. For the second solution, Fig. 6b, a flow pattern akin to that of Fig. 5d, is obtained through gradually decreasing $U_L$ from 3.0 to 1.0. The results indicate that the flow structure of Fig. 6b remains approximately symmetrical to that of Fig. 6a, illuminating by the values of AU and UC. For the third solution, Fig. 5c, the air flow rate FR is reduced when compar-

ing with the aforementioned non-symmetrical solutions of Fig. 6a and b. The symmetrical flow structure can be maintained when the left jet flow is perturbed to 1.005 (not shown).

The effect of left jet flow $U_L$ on the average horizontal velocity along the jet axis AU and the $U$-component UC is depicted in Fig. 7a and b. In general, AU is an increasing function of $U_L$ when $U_L$ far exceeds unity, while it is a decreasing function of $U_L$ when $U_L$ is much less than unity. For the former situation, UC positively increases with $U_L$ and counter-clockwise flow dominates. As the left jet decays from higher values (such as $U_L = 3.0$) to lower values, similar flow structures can be maintained, but the flow intensity and the space occupied by the main eddy are reduced. The steady solutions could be maintained for $0.9 \leqslant U_L \leqslant 3.0$. For the latter situation, the value of UC changes little and clockwise flow dominates. As the left jet flow strengthens from lower values (such as $U_L = 0$, Fig. 5a) to higher values, the flow intensity of the main eddy dominated by the right jet flow also reduces. The steady solutions corresponding to the latter situation could be maintained for $0 \leqslant U_L \leqslant 1.1$. For the equal–opposite jet flow, around $U_L = 1$, AU should theoretically approach zero. Simultaneously, the symmetrical flow structures are sensitive to the initial conditions and perturbations as observed from Fig. 5c. Therefore, the flow structure similar to Fig. 5c could be sustained only for $0.977 \leqslant U_L \leqslant 1.026$ ($1.466 \leqslant u_L \leqslant 1.539$ m/s).

For the flow rate $FR$, as indicated in Fig. 7c, it is generally an increasing function of $U_L$. Particularly, the flow rate of the third possible solution is reduced greatly, and lower than other solutions.

### 6.2. Effect of enclosure width

Firstly, the effect of $W/H$ on the unique steady flows is investigated. The right air jet could readily reach to the opposite wall and its inertial momentum force is much strong to completely inhibit the spread of left jet for $W/H = 0.7$ and $U_L = 0.5$ ($u_L = 0.75$ m/s), as presented in Fig. 8a. Subsequently, the main flow induces two circulations separated by the right jet flow in XOZ mid-plane, one is the clockwise flow eddy above the blowing level, and the other is the reverse flow induced in the layer between the jet axis and the floor. Comparing with that of $W/H = 1.5$ shown in Fig. 5b, both flow eddies reduce in size and strengthen in intensity due to the axial distance of jet flow decreases. As shown in Fig. 8b, the right jet for $W/H$ increasing up to 2.3 spreads over a longer distance and the velocity decay is greater than that of $W/H = 1.5$. Consequently, the interface of opposite jets shifts right and approaches to the vertical central plane $X = 0$. When the air-supply velocity of the left jet flow is triple high, $U_L = 1.5$, the higher momentum entrains the room air near the left port and the overall air velocities at the floor level are larger shown in Fig. 8c and d. As a consequence, a large amount of room air is entrained such that eddies in the corners of the rear wall become bigger. For the slender enclosure, $W/H = 0.7$, the whole flow structure presented in Fig. 8c has been re-

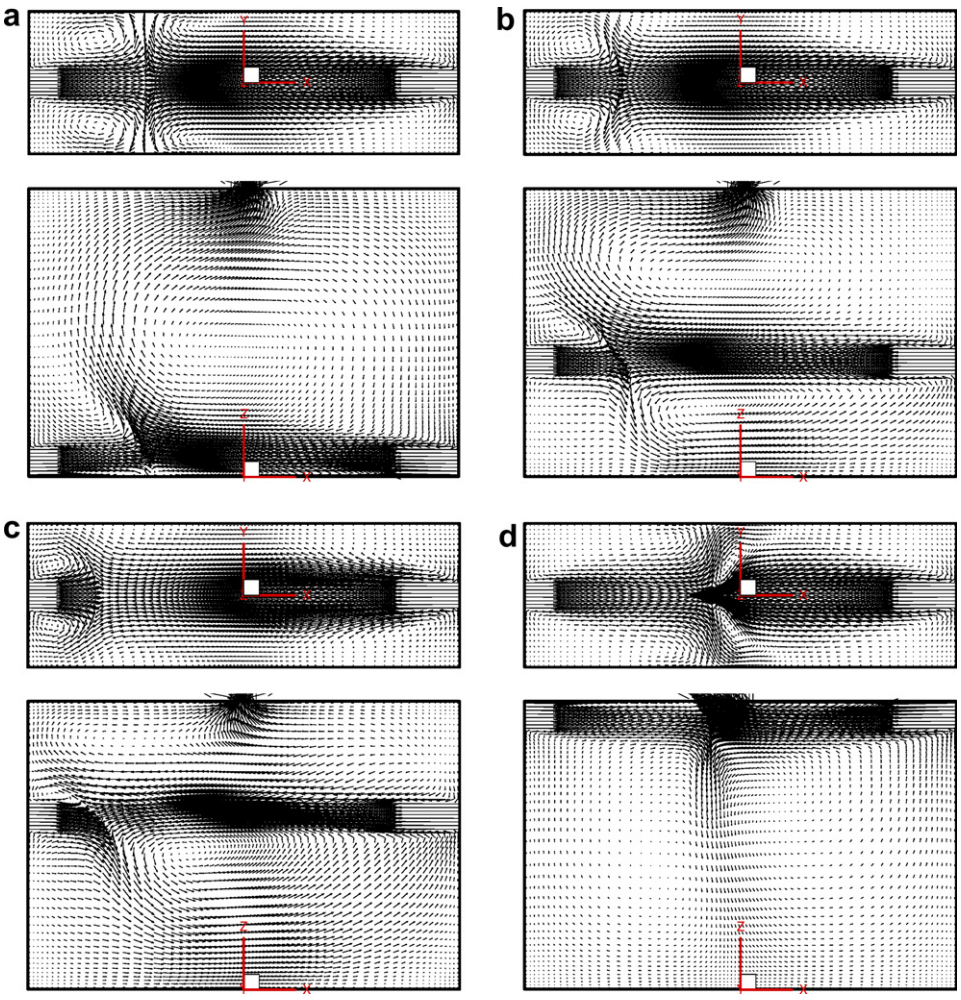


**Fig. 11.** Effect of $C$ on the steady vector flow for $Re = 2 \times 10^5$, $W/H = 1.50$ and $U_L = 0.5$. (a) $C/H = 0.05$, AU = −0.4582, UC = −0.6895, FR = 0.0000; (b) $C/H = 0.40$, AU = −0.4947, UC = −0.6796, FR = 0.0164; (c) $C/H = 0.60$, AU = −0.4190, UC = −0.4411, FR = 0.0350 and (d) $C/H = 0.95$, AU = −0.3277, UC = −0.6220, FR = 0.0113.

versed from that shown in Fig. 8a. However, for the shallow enclosure, $W/H = 2.3$, the flow pattern shown in Fig. 8d is almost similar to that in Fig. 8b, excluding that the interface of jet flows shifts to the right side of the vertical mid-plane $X = 0$.

Secondly, the enclosure width can affect the multiple steady flow states significantly. Fig. 9 presents the multiple steady solutions for $W/H = 1.2$ and $U_L = 1.0$. The first solution, Fig. 9a, obtained by using the flow pattern of $U_L = 0.0$ as initial conditions, is observed that the jet interface shifts to the left side of vertical mid-plane $X = 0$. For the second solution, Fig. 9b, is obtained through gradually decreasing $U_L$ from higher value 2.0 to 1.0, and the interface of jet flows is observed to shift to the right side of mid-plane $X = 0$. Correspondingly, the signs of AU and UC are opposite to those of the first solution. Apart from the non-symmetrical solutions, the symmetrical solution presented in Fig. 9c is obtained using the rest state $U = V = W = 0$ as initial conditions. The general symmetric flow pattern, satisfying Eqs. (23a)–(23c), seems similar to that of $W/H = 1.5$ presented in Fig. 5c. However, closely scrutinizing the non-symmetrical steady solutions, the horizontal eccentricity of jet interface from the vertical mid-plane ($X = 0$) depends on the enclosure width.

Actually, the eccentricity of jet interface can also be illuminated by the corresponding values of AU. As shown in Fig. 10a, the average horizontal velocity along the jet axis AU has been described as a function of enclosure width $W/H$ with parameter $U_L = 1.0$. Generally, the flow pattern obtained from rest state maintains symmetrical structure, which results in that absolute value of AU asymptotically approaches to zero. It is noted from Fig. 10a that the marked non-symmetrical solutions obtained by using initial conditions of lower and higher $U_L$ values could be sustained for $0.9 < W/H < 1.8$, where the amplitude of AU is greater than 0.1 and with the prominent eccentricity of jet interface from mid-plane ($X = 0$). However, outside the range $0.9 < W/H < 1.8$, the spanwise between jet interface and the vertical mid-plane $X = 0$ shrinks, the solutions of non-symmetrical flow patterns are slightly different from the symmetrical solution, which substantially attenuates the amplitude of AU (<0.1).

The flow rate as a function of enclosure width has been presented in Fig. 10b with left jet flow $U_L$ as parameters. For steady solutions of $U_L = 0.5$ and $U_L = 1.5$, one can see that the flow rate FR first abruptly decays with increasing enclosure width due to the fact that the jet flow spreads wider and the momentum of induced room air at floor level becomes weak, with the increasing of enclosure width. However, after FR achieves a lower value around at $W/H = 1$, FR varies non-linearly with enclosure width, increasing first and thereafter decreasing as room expands in width.

For the multiple steady solutions of $U_L = 1.0$, flow rates of non-symmetrical solutions, respectively, represented by the diamond symbol (using initial conditions of $U_L = 2.0$) and the gradient symbol (using initial conditions of $U_L = 0.0$), are nearly identical due to these flow patterns exemplified in Fig. 6a, b and in Fig. 9a, b are symmetrical with each other. In the range of $0.9 < W/H < 1.8$, the

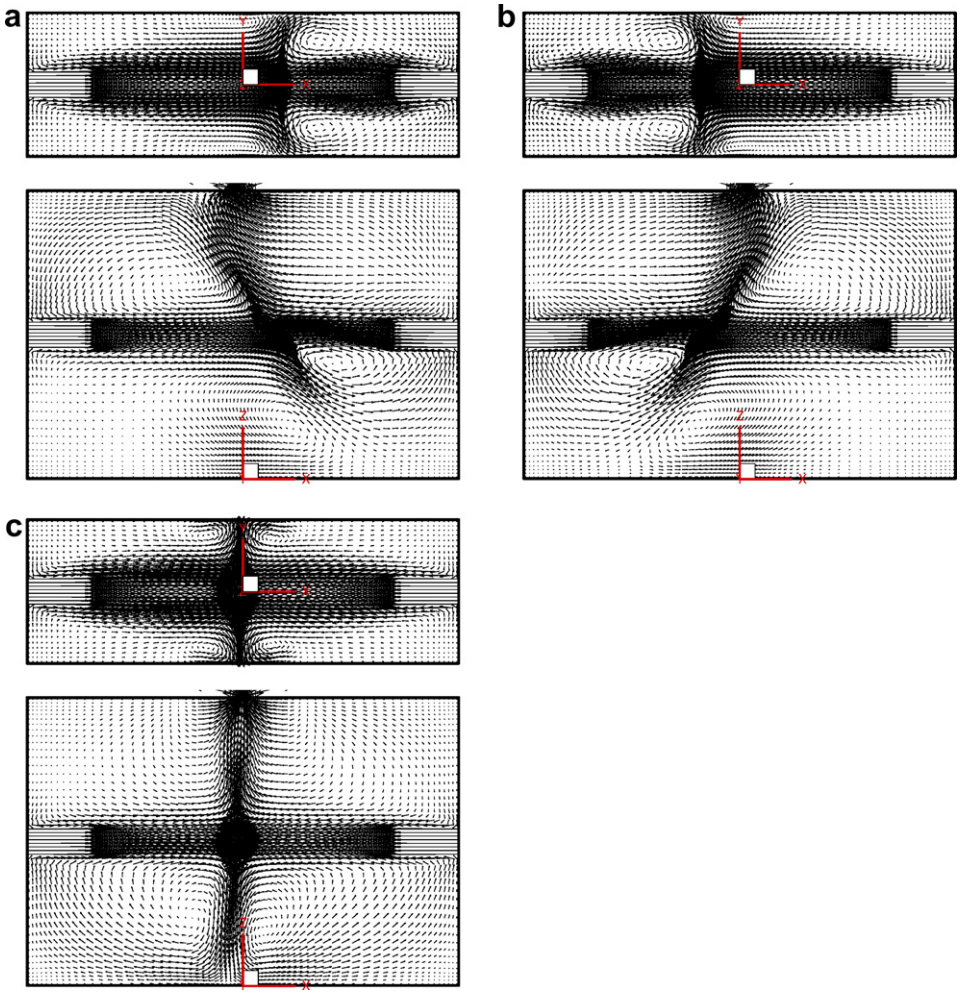


**Fig. 12.** Multiple vector flow charts for $Re = 2 \times 10^5$, $W/H = 1.5$ and $C/H = 0.50$. (a) $U_L = 1.0$, AU = 0.2048, UC = 0.6514, FR = 0.0255; (b) $U_L = 1.0$, AU = −0.2084, UC = −0.6607, FR = 0.0261 and (c) $U_L = 1.0$, AU = −0.0431, UC = −0.2638, FR = 0.0274.

flow rate of non-symmetrical solutions is significantly greater than that of symmetrical solutions represented by the delta symbol (using rest state as initial conditions). Particularly, for non-symmetrical solutions of $1.0 \leqslant W/H \leqslant 1.2$, flow rates can be enhanced greatly such that it exceeds the steady solution of $U_L = 1.5$. Outside the range of $0.9 < W/H < 1.8$, FR of $U_L = 1$ almost collapses into a unique value, being independent of initial conditions.

### 6.3. Elevation effect of supplying jet ports

The pitch between the center of the supplying ports and the floor has a significant impact on the flow pattern and air extraction. The present investigation assumes that enclosure width maintains at $W/H = 1.5$. As shown in Fig. 11a, $C/H = 0.05$, both jets spread over the floor and then rise along the interface set up by jet interaction in the room. Basically, the flow in XOZ mid-plane consists of a clockwise vortex occupying most of the enclosure and an anticlockwise circulation adjacent to the left wall. The flow rate flowing in and out of the volume $Vol_Z$ decreases to zero due to the fact that the downward side of supplying ports coincides with the floor. As the supplying ports are elevated to $C/H = 0.25$, shown in Fig. 5b, both jets spread transversely and induce multi-cell vortexes in vertical XOZ mid-plane, while the vector structure on XOY plane at the blowing axis remains unchanged from that of $C/H = 0.05$. Similar flow structure can be observed in Fig. 11b for $C/H = 0.40$ with the vortexes below the blowing axis enlarging and those above it shrinking. As the supplying ports are further elevated up to $C/H = 0.60$, presented in Fig. 11c, the left jet flow seems to be supplied at some angle downward along the blowing interface squeezed by the right jet flow of high momentum. Thus, the better mixing below the blowing axis could be achieved. Correspondingly, the flow rate has been considerably enhanced to 0.035, nearly two times greater than that of $C/H = 0.40$. When the upward side of the supplying ports touches the top wall, $C/H = 0.95$, as presented in XOZ mid-plane of Fig. 11d, the multi-cell pattern emerging evolves into bi-cellular flow below the jet flow axis. Particularly, the right jet flow is observed to abruptly decay at the outlet. Comparing with the flow pattern of $C/H = 0.6$, the left jet flow seems to own enough momentum to protrude and reach to the vertical mid-plane $X = 0$. As observing from vector flows in horizontal XOY plane at blowing axis, the vortexes induced by the left jet grow in size and strength, while the cells induced by the right jet flow are confined in the vicinity of lateral walls. Actually, the comparative adverse pressure gradient annularly around the exhaust port accelerates the decay of the flow of higher momentum, which starts to exert influence resulting in the complicated flow pattern in XOY blowing plane disclosed in Fig. 11d.

Apart from the aforementioned unique solutions, the elevation of supplying ports could also affect the multiple steady flow states. For instance, Fig. 12a–c illustrate three different possible solutions for $C/H = 0.5$ and $U_L = 1.0$. The first solution (Fig. 12a) and the second solution (Fig. 12b) are obtained, respectively, by using the flow configurations of $U_L = 0.0$ and $U_L = 2.0$ as initial conditions. For the third solution, an approximately symmetrical flow pattern is shown in Fig. 12c, using the rest state as initial conditions. Unexpectedly, for the first (second) solutions, the left jet flow pushes the interface of blowing jets rightward (leftward) if the left jet is increased (decreased) from lower (higher) value to unity. This is due to the fact that the shortcut occurs between the higher supplying air port and exhaust port.

The average horizontal blowing velocity AU, numerical notation of jet interface shift, is depicted in Fig. 13a for $Re = 2 \times 10^5$, $U_L = 1.0$ and $0.05 \leqslant C/H \leqslant 0.95$. Multiple steady solutions are obtained by employing different initial conditions, including steady solutions of $U_L = 0.0$, $U_L = 2.0$ and rest state. Generally, the multiple steady solutions occur at $0.15 < C/H < 0.70$, with the AU amplitude of non-symmetrical solutions greatly exceeding 0.1. Here should be noted that, reverse solutions in the range of $0.35 \leqslant C/H < 0.70$ as depicted in Fig. 12 for $C/H = 0.5$, are also on account of shortcuts. Outside the range of $0.15 < C/H < 0.7$, the development of the wall jet is limited by the effect of both lateral and vertical confinement due, respectively, to the interaction of the mean flow with the lateral enclosure wall and with top wall or floor. This confinement effect reduces the entrainment of the jet with its surroundings and leads to stabilization of the airflow rate and leads the possible flow states into a single convective mode.

The flow rate FR as a function of supplying ports elevation has been illustrated in Fig. 13b for different $U_L$. Flow rates of steady solutions $U_L = 0.5$ and $U_L = 1.5$ almost parallel each other and present fluctuation of double-peak structure with supplying ports $C/H$. FR increases with promoting $C/H$ and firstly peaks around at $C/H = 0.2$ and then decays to $C/H = 0.35$ where the adverse pressure gradient adjacent to the exhaust port would comparably affect the horizontal blowing flow. Further increasing $C/H$ continuously, FR again increases abruptly and the maximum flow rate occurs around at $C/H = 0.7$. Subsequently, FR decays with the promotion

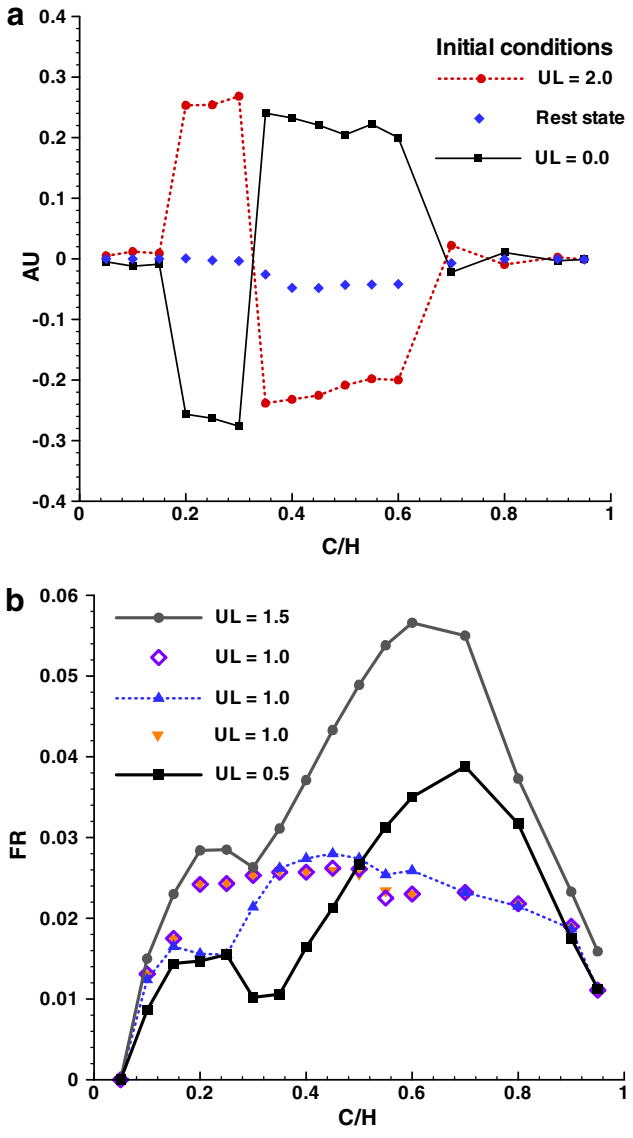


**Fig. 13.** Average blowing velocity AU and flow rate FR as functions of supplying ports elevation $C/H$ with parameter $U_L$, and $Re = 2 \times 10^5$. (a) AU as a function of $C/H$ for $U_L = 1.0$; (b) FR as a function of $C/H$.

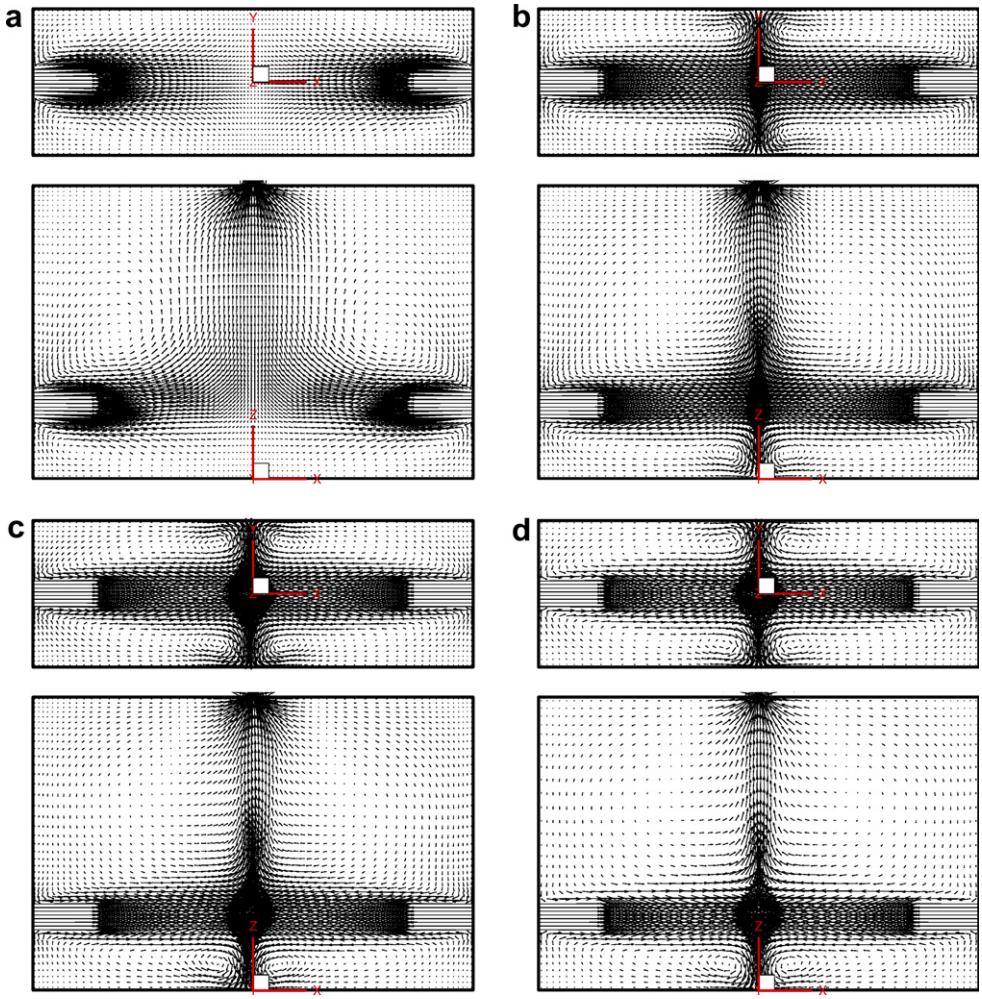


**Fig. 14.** Airflow patterns for $W/H = 1.5$, $C/H = 0.25$ and $U_L = 1.0$. (a) $Re = 2.5 \times 10^2$, AU = 0.0004, UC = 0.0007, FR = 0.0072; (b) $Re = 10^3$, AU = −0.0011, UC = −0.0077, FR = 0.0124; (c) $Re = 10^4$, AU = −0.0020, UC = −0.0165, FR = 0.0152 and (d) $Re = 8.0 \times 10^5$, AU = −0.0044, UC = −0.0230, FR = 0.0158.

of supplying ports. For the situations of equal-intensity supplying jets ($U_L = 1.0$), that of symmetrical solutions represented by the delta symbol (using rest state as initial conditions) firstly increases with $C/H$, and almost flats at $0.2 < C/H < 0.8$. Similar trends can be found for the flow rates of non-symmetrical solutions, respectively, represented by the diamond symbol (using initial conditions of $U_L = 2.0$) and the gradient symbol (using initial conditions of $U_L = 0.0$).

### 6.4. Effect of Reynolds number

In order to analyze the effect of Reynolds number on the enclosure flow, geometries and left supplying velocity are maintained constants, $W/H = 1.5$, $C/H = 0.25$, $U_L = 1.0$ ($U_L = U_R$). As mentioned earlier, the right supplying velocity $u_R$ is in a range of $7.5 \times 10^{-4}$ m/s to 7.5 m/s, resulting in Reynolds number varies from $10^2$ to $10^6$, which essentially expresses the relative importance of inertial forces and viscous forces. When Reynolds number is small ($Re = 2.5 \times 10^2$), the jet flow is much weak, shown in Fig. 14a. It expands with an angle of about 15° and entrains the surrounding air. Between the inlet port and the interface of jets, the airflow rate increases and the decay of the maximum velocity of the jet is similar to an unbounded three-dimensional wall jet. Further downstream, the jet decreases faster until its collision. Within the enclosure, the development of the wall jet is limited by the effect of both lateral and vertical confinement, respectively, due to the interaction of the mean flow with the lateral enclosure wall and with reverse flow in the direction of the outlet. Particularly, with increasing strength of

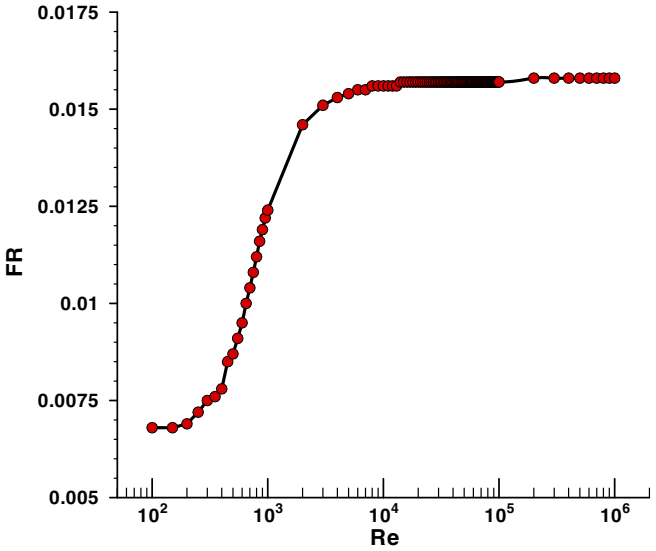


**Fig. 15.** Variations of flow rate as a function of Reynolds number with $U_L = U_R = 1.0$.

both jet flows ($Re = 10^3$, $u_R = 7.5 \times 10^{-3}$ m/s), shown in Fig. 14b, the entrainment of the right and left jets, respectively, with their surroundings is reduced and finally resulted in the stabilization of the airflow rate. Due to the equal-magnitude jets, the flow structures on the planes XOY and XOZ are both seen to symmetrical from $X = 0$. Particularly, similar flow structures are maintained till Reynolds number exceeds $10^3$. As a result, the flow plots of Figs. 14b–d and 5c and are seen almost unchanged except the flow intensity increases continuously and the path of jet flows becomes narrower. Additionally, the equal-magnitude opposite jet flow is intrinsically instable, particularly for high Reynolds number flows. Thus, the time-average values of AU and UC velocities cannot be compared directly.

As shown in Fig. 15, the volume flow rate *FR* is enhanced greatly as *Re* increases from $10^2$ to $10^4$. However, *FR* increases little as Reynolds number further increases. Similar flow patterns and associated causes can be found in Fig. 14.

## 7. Conclusions

A three-dimensional airflow numerical model is developed based on atmospheric convection diffusion equation and RSM turbulence model to predict the air motion within an enclosure employing two-opposite slotted openings. Multiple steady solutions are particularly concerned in terms of inlet velocity, enclosure width, and elevation of supplying ports.

The velocity of left jet affects the airflow pattern and velocity characteristics in this enclosure. The existence of three different flow patterns is demonstrated for $Re = 2.0 \times 10^5$, $W/H = 1.5$ and $C/H = 0.25$. The counter-clockwise flow and clockwise flow on vertical XOZ mid-plane could be maintained, respectively, for $0.90 \leqslant U_L \leqslant 3.00$ and $0.00 \leqslant U_L \leqslant 1.10$; for the third solution, the symmetrical flow structures obtained from rest states could be sustained only for $0.977 \leqslant U_L \leqslant 1.026$. The flow rate of non-symmetrical solutions is significantly greater than that of symmetrical solutions.

Enclosure width would affect the flow states of unique and multiple steady solutions. Airflow eddies enlarge in size and reduce in intensity with the increasing enclosure width. The marked multiple steady solutions obtained by using initial conditions of lower and higher $U_L$ values could be sustained for $0.9 < W/H < 1.8$, where prominent eccentricity of jet interface occurs. Variation profiles of flow rate with enclosure width are non-linear, depending on the supplying velocity and initial conditions.

The pitch between the center of the supplying ports and the floor has a significant impact on the flow pattern and air extraction. Generally, the multiple steady solutions occur at $0.15 < C/H < 0.70$, where the AU amplitude of non-symmetrical solutions greatly exceeds 0.1. Flow rates of unique solutions present fluctuation of double-peak structure with supplying ports $C/H$. However, for the situations of equal-intensity supplying jets, flow rates vary slightly with the port elevation.

As the Reynolds number is small ($<10^4$), the flow has the distinctive characteristics of a jet. After Reynolds number exceeds $10^3$, the flow pattern changes slightly. The volume flow rate increases with Reynolds number increasing from $10^2$ to $10^4$, and approaches approximately constant as Reynolds number increases further.

Only CFD method has been adopted in present work for limitations, whereas, the stability analysis and experimental validation of the multiple steady flows would be conducted in our further studies due to the fact that they could give physical insight into the fluid mechanics and possible flow solutions.

## Acknowledgements

This research work was financially supported by a Grant from the Natural Science Foundation of China (NSFC No. 50578059). The authors are also grateful to the anonymous referees who provided constructive and valuable comments.

## References

Aidun, C.K., Triantafillopoulos, N.G., Benson, J.D., 1991. Global stability of a lid-driven cavity with through flow: flow visualization studies. Physics of Fluids A 3, 2081–2091.

Bilgen, E., Yamane, T., 2004. Conjugate heat transfer in enclosures with openings for ventilation. Heat and Mass Transfer 40, 401–411.

Bourich, M., Amahmid, A., Hasnaoui, M., 2004a. Double diffusive convection in a porous enclosure submitted to cross gradients of temperature and concentration. Energy Conversion and Management 45, 1655–1670.

Bourich, M., Hasnaoui, M., Amahmid, A., 2004b. Double-diffusive natural convection in a porous enclosure partially heated from below and differentially salted. International Journal of Heat Fluid Flow 25, 1034–1046.

Calmidi, V.V., Mahajan, R.L., 1998. Mixed convection over a heated horizontal surface in a partial enclosure. International Journal of Heat Fluid Flow 19, 358–367.

Chen, Q., 1995. Comparison of different $k$–$\varepsilon$ models for indoor air flow computations. Numerical Heat Transfer, Part B 28, 353–369.

Chen, Q., 1996. Prediction of room air motion by Reynolds-stress models. Building and Environment 31, 233–244.

Chen, W., Zhao, F.Y., Tang, G.F., Liu, D., 2006. Transportation of indoor double diffusive mixed convection coupled with diffusion in solid walls. Journal of HV&AC 36, 12–18.

Craft, T.J., Graham, L.J.W., Launder, B.E., 1993. Impinging jet studies for turbulence model assessment—II. An examination of the performance of four turbulence models. International Journal of Heat Mass Transfer 36, 2685–2697.

Hanjalic, K., Launder, B.E., 1976. Contribution towards a Reynolds-stress closure for low-Reynolds-number turbulence. Journal of Fluid Mechanics 74, 593–610.

Hayase, T., Humphrey, J.A.C., Greif, R., 1992. A consistently formulated QUICK scheme for fast and stable convergence using finite-volume iterative calculation procedure. Journal of Computational Physics 98, 108–118.

Koseff, J.R., Street, R.L., 1984. The lid-driven cavity flow: a synthesis of qualitative and quantitative observations. ASME Journal of Fluid Engineering 106, 390–398.

Kuhlmann, H.C., Wanschura, M., Rath, H.J., 1997. Flow in two-sided lid-driven cavities: non-uniqueness, instabilities and cellular structures. Journal of Fluid Mechanics 336, 267–299.

Launder, B.E., 1988. On the computation of convective heat transfer in complex turbulent flows. ASME Journal of Heat Transfer 110, 1112–1128.

Launder, B.E., Spalding, D.B., 1974. The numerical computation of turbulent flows. Computer Methods in Applied Mechanics and Engineering 3, 269–289.

Launder, B.E., Reece, G.J., Rodi, W., 1975. Progress in the development of a Reynolds stress turbulence closure. Journal of Fluid Mechanics 68, 537–566.

Lien, F.S., Leschziner, J., 1994. Assessment of turbulent transport models including non-linear RNG eddy-viscosity formulation and second-moment closure. Computers & Fluids 23, 983–1004.

Li, Y., Xu, P., Qian, H., Deng, Q.H., Wu, J., 2006. Flow bifurcation due to opposing buoyancy in two vertically connected open cavities. International Journal of Heat Mass Transfer 49, 3298–3312.

Liu, D., Zhao, F.Y., Tang, G.F., 2008a. Numerical analysis of two contaminants removal from a three-dimensional cavity. International Journal of Heat Mass Transfer 51, 378–382.

Liu, D., Zhao, F.Y., Tang, G.F., 2008b. Conjugate heat transfer in an enclosure with a centered conducting body imposed sinusoidal temperature profiles on one side. Numerical Heat Transfer, Part A 53, 204–223.

Liu, D., Zhao, F.Y., Tang, G.F., 2008c. Thermosolutal convection in a saturated porous enclosure with concentrated energy and solute sources. Energy Conversion and Management 49, 16–31.

Mahmud, S., Pop, I., 2006. Mixed convection in a square vented enclosure filled with a porous medium. International Journal of Heat Mass Transfer 49, 2190–2206.

Mamou, M., 2002. Stability analysis of thermosolutal convection in a vertical packed porous enclosure. Physics of Fluids 14, 4302–4314.

Mamou, M., Vasseur, P., Bilgen, E., 1995. Multiple solutions for double-diffusive convection in a vertical porous enclosure. International Journal of Heat Mass Transfer 38, 1787–1798.

Mamou, M., Vasseur, P., Bilgen, E., 1998. Double-diffusive convection instability in a vertical porous enclosure. Journal of Fluid Mechanics 368, 263–289.

Moureh, J., Flick, D., 2003. Wall air-jet characteristics and airflow patterns within a slot ventilated enclosure. International Journal of Thermal Sciences 42, 703–711.

Moureh, J., Flick, D., 2004. Airflow pattern and temperature distribution in a typical refrigerated truck configuration loaded with pallets. International Journal of Refrigeration 27, 464–474.

Moureh, J., Flick, D., 2005. Airflow characteristics within a slot-ventilated enclosure. International Journal of Heat Fluid Flow 26, 12–24.

Moureh, J., Menia, N., Flick, D., 2002. Numerical and experimental study of airflow in a typical refrigerated truck configuration loaded with pallets. Computers and Electronics in Agriculture 34, 25–42.

Papanicolaou, E., Jaluria, Y., 1992. Transition to a periodic regime in mixed convection in a square cavity. Journal of Fluid Mechanics 239, 489–509.

Papanicolaou, E., Jaluria, Y., 1995. Computation of turbulent flow in mixed convection in a cavity with a localized heat source. ASME Journal of Heat Transfer 117, 649–658.

Patankar, S.V., 1980. Numerical Heat Transfer and Fluid Flow. Hemisphere, Washington, DC.

Stone, H.L., 1968. Iterative solution of implicit approximations of multidimensional partial differential equations. SIAM Journal on Numerical Analysis 5, 530–558.

Tapsoba, M., Moureh, J., Flick, D., 2007. Airflow patterns inside slotted obstacles in a ventilated enclosure. Computers & Fluids 36, 935–948.

Versteeg, H.K., Malalasekera, W., 1999. An introduction to computational fluid dynamics: the finite volume method. Addison-Wesley, Longman Limited, Harlow.

Zhao, F.Y., Tang, G.F., Liu, D., 2006.Conjugate natural convection in enclosures with external and internal heat sources. International Journal of Engineering Science 44, 148–165.

Zhao, F.Y., Liu, D., Tang, G.F., 2007a. Multiple steady flows in confined gaseous double diffusion with discrete thermosolutal sources. Physics of Fluids 19, 107103.

Zhao, F.Y., Liu, D., Tang, G.F., 2007b. Application issues of the streamline, heatline and massline for conjugate heat and mass transfer.International Journal of Heat Mass Transfer 50, 320–334.

Zhao, F.Y., Liu, D., Tang, G.F., 2007c. Conjugate heat transfer in square enclosures. Heat and Mass Transfer 43, 907–922.

Zhao, F.Y., Liu, D., Tang, G.F., 2007d. Free convection from one thermal and solute source in a confined porous medium. Transport in Porous Media 70, 407–425.

Zhao, F.Y., Liu, D., Tang, G.F., 2007e. Resonant response of fluid flow subjected to discrete heating elements. Energy Conversion and Management 48, 2461–2472.

Zhao, F.Y., Liu, D., Tang, G.F., 2008a. Natural convection in an enclosure with localized heating and salting from below. International Journal of Heat Mass Transfer 51, 2889–2904.

Zhao, F.Y., Liu, D., Tang, G.F., 2008b. Natural convection in a porous enclosure with a partial heating and salting element. International Journal of Thermal Sciences 47, 569–583.